Available online at www.sciencedirect.com
ScienceDirect
Journal of the European Ceramic Society 30 (2010) 2905–2915
www.elsevier.com/locate/jeurceramsoc

Effect of yttria doping on the microstructure and mechanical properties of Al_2O_3–$FeAl_2O_4$ nanocomposites developed via solid state precipitation

Amartya Mukhopadhyay, Richard I. Todd *

University of Oxford, Department of Materials, Parks Road, Oxford OX1 3PH, UK

Available online 8 June 2010

Abstract

We have recently reported the production of Al_2O_3-matrix nanocomposites via solid state precipitation of nanosized $FeAl_2O_4$ particles within the matrix grains during aging of Al_2O_3–10 wt.% Fe_2O_3 solid solutions in a reducing atmosphere ($N_2 + 4\%$ H_2). In addition to these nanoparticles, however, coarse micron-sized $FeAl_2O_4$ particles were present along the matrix grain boundaries. In the present work, we show that the addition of ~250 ppm yttria to the solid solutions suppressed the development of these intergranular particles, reducing their size by a factor of ~2 with optimum aging. A fracture toughness improvement by 45% and flexural strength improvement by 50% with respect to monolithic Al_2O_3 were recorded with the yttria-containing nanocomposite developed by aging for 20 h at 1450 °C. Aging also improved the hardness with respect to the solid solution. The change in fracture mode in the presence of the nanosized intragranular particles was believed to be the major contributing factor towards the improvement in toughness and therefore the strength. The higher strengths obtainable in the presence of yttria were attributed to the reduction of intergranular precipitate size relative to yttria-free nanocomposites.

Keywords: Nanocomposite; Processing; Microstructure; Mechanical properties

1. Introduction

Ceramic nanocomposites are characterised by at least one of the microstructural phases having dimensions less than ~100 nm. Research over the last decade has unambiguously demonstrated that ceramic nanocomposites possess significantly improved mechanical and tribological properties with respect to monolithic ceramics or conventional composites with coarser microstructural scale.[1–11] Considering that monolithic Al_2O_3 is already used extensively for structural and wear resistant applications, it is clear that there is potential commercial advantage in developing high performance Al_2O_3-based ceramic nanocomposites, as well as academic interest.

Niihara[1] reported for the first time that Al_2O_3–SiC nanocomposites, comprising nanosized SiC particles dispersed in a matrix of micron-sized Al_2O_3 grains, are significantly stronger than monolithic Al_2O_3. Subsequently, various research groups reported that such nanocomposites also possess significantly improved wear resistance.[5–7,10,11] However, it has also been found that it is very difficult to densify such nanocomposites via conventional pressureless sintering[2–4,7,9] because the incorporation of covalent SiC, with its low diffusion co-efficient, severely inhibits sintering.[2–4,9] However, when second phase oxide nanoparticles are incorporated, which are more conducive to sintering, they tend to coarsen during densification, so that the nanostructure is destroyed.[2,3,12] Although there has been some success with the use of sintering aids with SiC[13,14] or particles of more refractory oxides such as mullite,[15,16] this has not been sufficient to enable the potential benefits of the nanocomposite microstructure to be realised with pressureless sintering.

For these reasons, most alumina-based nanocomposites have been made on a laboratory scale using hot pressing or SPS.[1–9] Such techniques are not suitable for commercial production because, apart from being very expensive, they are not suitable for continuous batch production and also severely limit the shape and size of the components that can be produced.[2–4] Hence, despite being such promising materials, the processing difficulties have severely hindered their commercial exploitation.

An alternative avenue for developing such nanocomposites is to densify the ceramic as a single phase solid solution based on alumina and then to precipitate the nanoparticles by changing the oxidation state of the solute cations. However, due to

* Corresponding author. Tel.: +44 1865 273718; fax: +44 1865 273783.
E-mail addresses: richard.todd@materials.ox.ac.uk, jecsmat@herald.ox.ac.uk (R.I. Todd).

0955-2219/$ – see front matter © 2010 Elsevier Ltd. All rights reserved.
doi:10.1016/j.jeurceramsoc.2010.04.024

the limited solubility of most cations in Al_2O_3 and the difficulty of nucleating second phase particles within the alumina grains, most previous reports which explore this possibility have not been able to develop a sufficient volume fraction of well dispersed nanoparticles to establish reproducible property improvements.[17,18] Recently, however, we have reported the production of viable nanocomposites by using Fe_2O_3 solid solutions in Al_2O_3.[19,20] Fe_2O_3 (haematite) has the same crystal structure as α-Al_2O_3 (corundum) and possesses substantial solubility in Al_2O_3 at moderately high temperatures in air (~15 wt.% at ~1410 °C).[21] This allowed the development of dense polycrystalline solid solutions of Al_2O_3–10 wt.% Fe_2O_3 during pressureless sintering in air. Aging of the fully dense solid solutions in a reducing atmosphere led to the precipitation of $FeAl_2O_4$ particles in the Al_2O_3 matrix. Under optimised aging conditions, nanosized precipitate particles (~80 nm) were formed within the grains (intragranular particles). However, coarser micro-scale particles were also present along the matrix grain boundaries and triple point corners (intergranular particles). These are potentially detrimental to the mechanical properties and it is important for their size and volume fraction to be limited.

Although the ease of heterogeneous particle nucleation at grain boundaries and the high rate of grain boundary diffusion compared with that in the lattice make it unlikely that these intergranular particles can be completely eliminated, it may be possible to limit their development by using dopants to inhibit grain boundary diffusion. It is now well known that some dopants, such as yttria or lanthana, substantially reduce grain boundary diffusion co-efficients in alumina[22–26] as is shown by reduced rates of creep and sintering in their presence. The present work therefore explores the possibility that Y_2O_3 doping can suppress the development of coarse second phase particles along the grain boundaries during precipitation of $FeAl_2O_4$ to yield a viable production route for strong and wear resistant alumina-matrix nanocomposites by conventional shaping and pressureless sintering. The room temperature mechanical properties of the nanocomposites developed on aging the yttria-free and the yttria-doped solid solutions have also been investigated and discussed in terms of the microstructural development.

2. Experimental procedure

2.1. Processing

α-Al_2O_3 powders (99.995% purity; AKP50, Sumitomo, Japan) of mean particle size ~0.2 μm were used as the starting material for the matrix (Al_2O_3). In order to prevent abnormal grain growth during sintering and to enable near theoretical densification, the Al_2O_3 powders were doped with 250 ppm of MgO using pure MgO powders (99.95%; 120 nm; UBE, Japan).[27] The MgO doped Al_2O_3 powders were dispersed in ethanol using an ultrasonic probe. Fe^{3+} was incorporated by adding a solution of $Fe(NO_3)_3{\cdot}9H_2O$ (Sigma–Aldrich, UK, purity > 98%) in ethanol to the alumina slurries. The $Fe(NO_3)_3$ solutions contained an amount of the salt corresponding to 10 wt.% Fe_2O_3 in Al_2O_3 after calcination. In order to study the effect of Y_2O_3 doping (250 ppm by weight) on the microstructural developments, the requisite amounts of $Y(NO_3)_3{\cdot}6H_2O$ dissolved in ethanol were also added to some of the slurries. Pure alumina slurries were also made for comparison. All the slurries were ball milled for 24 h in bottles made of polyethylene, using high purity (99.99%) alumina balls. After ball milling the slurries were dried on a hot plate with constant stirring, using a magnetic stirrer. The dried powders were ground in an Al_2O_3 mortar and pestle and passed through a 150 μm sieve. Green compacts were produced by uniaxial cold pressing of the powders into 20 mm discs at 100 MPa, which were then sintered via pressureless sintering at 1450 °C for 5 h in air inside an alumina tube furnace (Lenton, UK). After sintering, the samples were then 'quenched' by pushing them immediately to the end of the furnace tube using an alumina rod. The Al_2O_3 samples containing 10 wt.% Fe_2O_3 will henceforth be referred to as 'A10F' and the samples additionally doped with Y_2O_3 (250 ppm) will be referred to as 'A10FY'. The supersaturated solid solutions were then aged in a tube furnace with capped ends in a $N_2 + 4\%$ H_2 forming gas mixture at 1450 and 1550 °C for different durations (up to 20 h). Lower temperatures were not investigated because microstructural development was too slow to be of practical use.[19] More details about the processing are mentioned elsewhere.[19,20]

2.2. Investigation of phase evolution and microstructural development

The sintered densities of all the samples were measured in distilled water according to Archimedes' principle. For phase identification and microstructural characterization, the samples were ground and polished using 25, 6, 3, 1 and 0.25 μm diamond slurries in order to remove the external surfaces and produce optically reflective ceramographic surfaces representative of the sample cores. X-ray diffraction (XRD; Philips, Netherlands) was performed using Cu K_α radiation at a collection rate of 3°/min. In order to reveal the grain boundaries of the as-sintered pure Al_2O_3 and A10F solid solution samples, thermal etching was done at a temperature of 1400 °C for 15 min in air. The microstructures of all the polished surfaces were observed using a field emission scanning electron microscope (JEOL 6500F) operated at 20 kV. Volume fractions of the second phase particles were determined via point counting on back scattered electron (BSE) images and the average particle sizes were determined from the mean of the major and minor axes of at least 20 particles, multiplied by 1.27 to obtain equivalent spherical diameters.[5,6,19] Sample preparation for transmission electron microscope (TEM) observations involved mechanical thinning of 3 mm discs, followed by ion-milling to electron transparency in a Gatan Duo Mill (5 kV). Observations were performed using a 200 kV JEOL 2000FX TEM, equipped with an EDS system.

2.3. Investigation of mechanical properties

Hardness was measured by Vickers indentation (H_v) on polished surfaces with an indentation load of 5 kg and loading time 15 s. Flexural strengths were measured using plain rectangular cross-section beams tested in four-point bending. The SEVNB

(Single Edge V-notch Beam) method was used to estimate the bulk fracture toughness of the nanocomposites and monolithic Al_2O_3. For the flexural strength and fracture toughness measurements, as-cut beams were polished on both narrow long faces and one broad long face using 25, 6, 3 and 1 μm diamond slurries. The final specimen dimensions were 13 mm × 2 mm × 2.5 mm. For SEVNB, the ratios between the notch depths and specimen thickness were between 0.2 and 0.3. The notches were sharpened by razor blade using diamond paste grades down to 1 μm so that the tip radii of the notches were less than ~10 μm. The flexural strengths and fracture toughnesses were measured in the four-point bending configuration, using a crosshead loading rate of 5 N/min and inner and outer spans of 5.8 and 10 mm, respectively. The tests were performed on a universal testing machine (Dension-Mayes, UK). For estimating the fracture toughness, the following relation was used:[28]

$$K_{Ic} = \frac{P_f(L_o - L_i)}{BW^{3/2}} \frac{3\alpha^{1/2}}{2(1-\alpha)^{3/2}} f(\alpha) \quad (1)$$

$$f(\alpha) = 1.9887 - 1.326\alpha - \frac{\alpha(1-\alpha)(3.49 - 0.68\alpha + 1.35\alpha^2)}{(1+\alpha)^2} \quad (2)$$

where P_f, L_o, L_i, B and W are experimentally measured fracture load, outer span, inner span, specimen width, and specimen depth, respectively. The pre-crack size (notch depth), a, enters the equation through α, where $\alpha = a/W$. The reported values are the averages of at least five independent measurements.

3. Results

3.1. Phase evolution and microstructure development

Pressureless sintering of pure Al_2O_3, A10F and A10FY resulted in densities of more than 98% of theoretical. No peaks other than those present in the XRD pattern obtained with monolithic alumina (α-Al_2O_3) (Fig. 1a) were observed in the XRD pattern corresponding to the as-sintered A10FY (Fig. 1b). The appearance of peaks corresponding to $FeAl_2O_4$ was observed after aging of the A10FY solid solution at 1450 and 1550 °C for 0 h or more in a reducing atmosphere (N_2 + 4% H_2 gas mixture) (Fig. 1c). Similar observations were made also with the yttria-free solid solution (A10F).[19]

No secondary phase was observed on the back scattered SEM images obtained from the polished and thermally etched surfaces of as-sintered monolithic Al_2O_3 (Fig. 2a) and A10FY (Fig. 2b) solid solutions. This confirms that the sintering step resulted in the formation of single phase polycrystalline solid solutions where Fe_2O_3 (~10 wt.%) and Y_2O_3 (~250 ppm) were completely dissolved in Al_2O_3. However, it was observed that doping with more than 250 ppm of yttria resulted in the precipitation of grain boundary particles of yttrium aluminium garnet. This is in agreement with earlier literature reports.[25] Hence the present investigations were carried on Al_2O_3–Fe_2O_3 solid solutions doped with ~250 ppm of yttria (A10FY). Similar mean grain sizes (~3 μm) were measured for monolithic alumina,

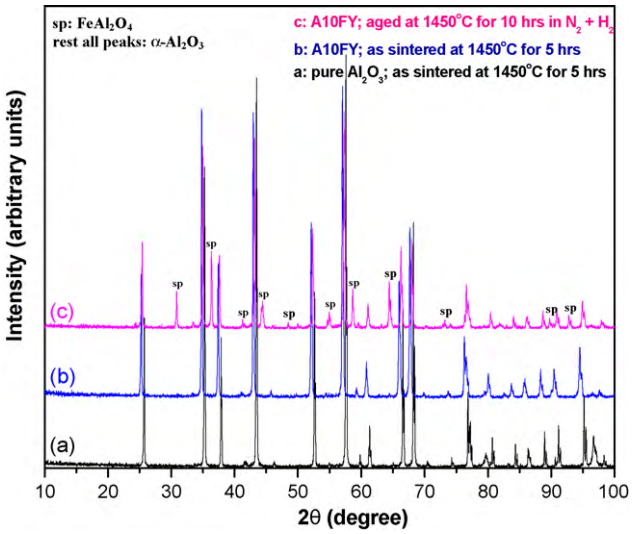

Fig. 1. X-ray diffraction (XRD) patterns recorded with ground and polished surfaces of (a) as-sintered monolithic Al_2O_3; (b) as-sintered Y_2O_3-containing Al_2O_3–10 wt.% Fe_2O_3 (A10FY) and (c) A10FY aged at 1450 °C for 10 h in N_2 + H_2.

A10F and A10FY, though a few grains in the solid solutions showed anisotropic growth, whereas all the grains in the monolithic Al_2O_3 were equiaxed.

The sequence of precipitation and coarsening of inter/intragranular second phase ($FeAl_2O_4$) particles with aging time

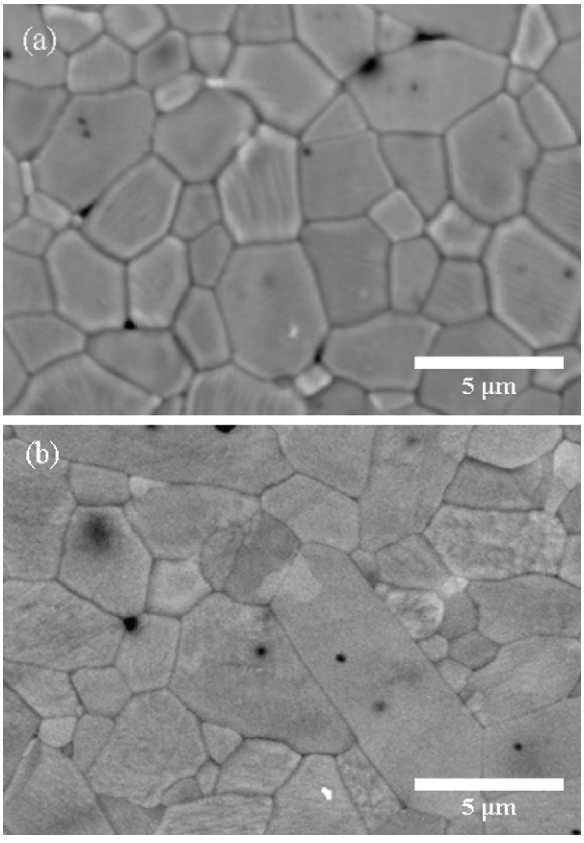

Fig. 2. SEM micrograph of polished and thermally etched surfaces of (a) pure Al_2O_3 and (b) A10FY solid solution.

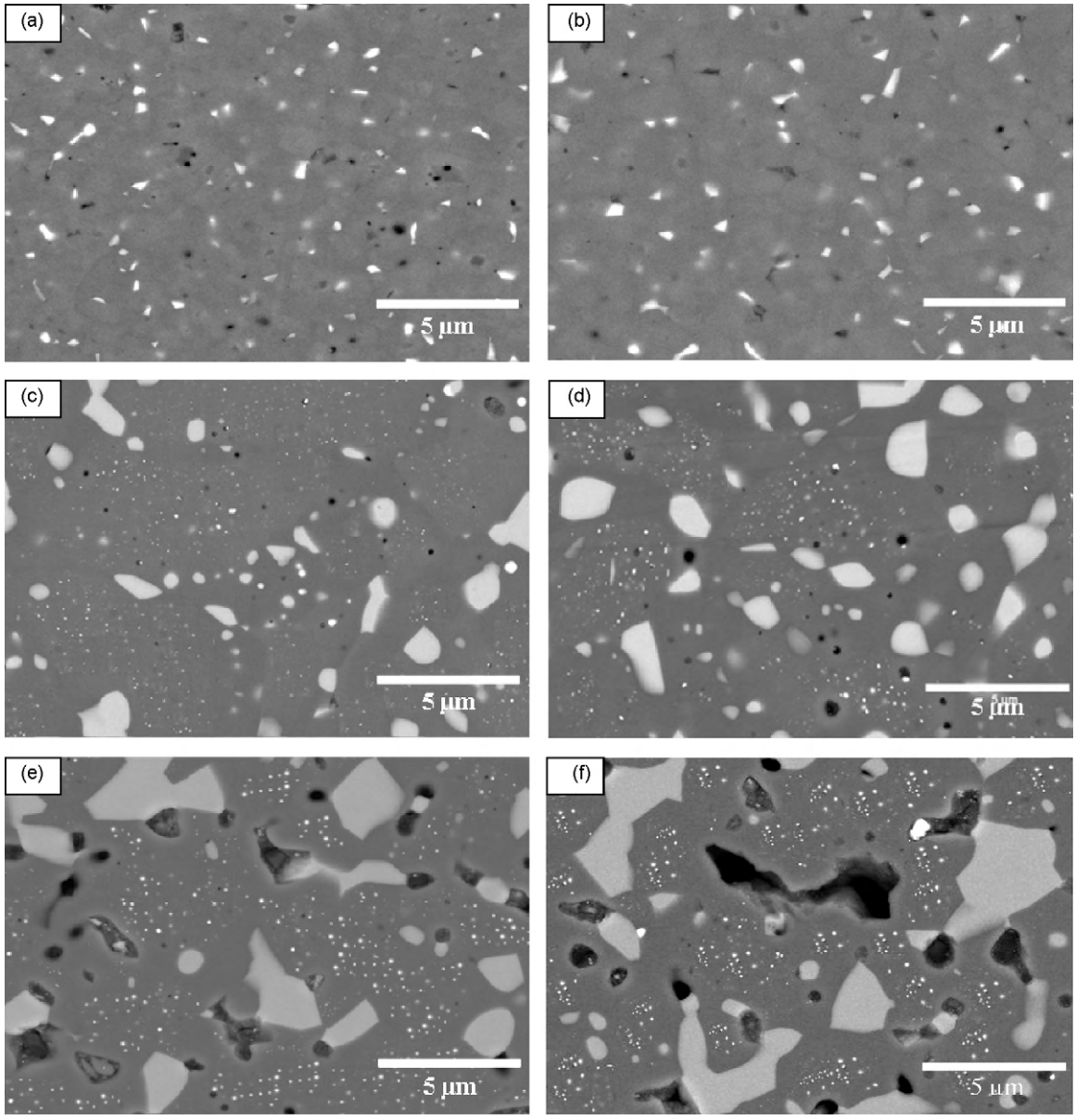

Fig. 3. Back scattered SEM (BSE-SEM) images corresponding to the bulk microstructural developments on aging of (a) A10FY solid solution (yttria-doped) at 1450 °C for 0 h; (b) A10F solid solution (yttria-free) at 1450 °C for 0 h; (c) A10FY at 1450 °C for 20 h; (d) A10F at 1450 °C for 20 h and (e) A10FY at 1550 °C for 10 h and (f) A10F at 1550 °C for 10 h.

were similar in the presence of yttria to those reported previously in its absence.[19] For comparison of the effect of yttria additions on the sizes of the precipitate particles, back scattered SEM (BSE-SEM) images obtained from ground and polished surfaces of A10F and A10FY, aged at 1450 and 1550 °C for different durations (0–20 h; where 0 h means that the specimen was heated to the specific temperature and cooled again without holding) in the reducing atmosphere, are shown in Fig. 3. The presence and average sizes of the inter- and intragranular second phase particles, as estimated from the BSE-SEM images, are also reported in Table 1. In the presence as well as in the absence of yttria,[19] a very thin surface layer (up to a thickness of ~40 μm) was observed where the $FeAl_2O_4$ was further reduced to α-Fe. However, no gradient in the amount and distribution of $FeAl_2O_4$ with sample thickness was observed for any of the aging schedules.

The most important result of the present work is the successful suppression of growth of the intergranular precipitate particles during reduction aging of the yttria-doped solid solutions (A10FY). It can be observed that during aging of A10FY only sub-micron-sized particles (mean diameter = 0.6 μm) appeared along the matrix grain boundaries after 0 h of aging at 1450 °C (Fig. 3a), as opposed to the micron-sized intergranular particles (mean diameter = 1.1 μm) that appeared initially (0 h) on aging of A10F (Fig. 3b) at the same temperature. Coarsening of the intergranular particles with aging duration was also hindered in the presence of yttria, such that the intergranular particles coarsened to an average size of ~1 μm after aging (of A10FY)

Table 1
Effects of yttria doping and sizes of the inter- and intragranular second phase ($FeAl_2O_4$) particles formed on aging of Al_2O_3–Fe_2O_3 solid solutions in reducing atmosphere ($N_2 + 4\%\ H_2$) at 1450 and 1550 °C.

Aging time (h)	Reduction aging temperature: 1450 °C				Reduction aging temperature: 1550 °C			
	Yttria-free		Yttria-doped		Yttria-free		Yttria-doped	
	Intergranular particle size (μm)	Intragranular particle size (nm)	Intergranular particle size (μm)	Intragranular particle size (nm)	Intergranular particle size (μm)	Intragranular particle size (nm)	Intergranular particle size (μm)	Intragranular particle size (nm)
0	1.1 ± 0.6	Not present	0.6 ± 0.3	Not present	2.9 ± 0.6	Not present	2.2 ± 0.4	27 ± 19
5	1.5 ± 0.8	Not present	0.7 ± 0.9	29 ± 7	5.4 ± 0.8	79 ± 17	4.8 ± 0.3	74 ± 11
10	1.7 ± 0.5	71 ± 27	0.9 ± 0.6	68 ± 14	Not measured due to excessive pull out	88 ± 19	Not measured due to excessive pull out	102 ± 16
15	1.9 ± 0.5	104 ± 38	1.2 ± 0.7	92 ± 11	Not measured due to excessive pull out	119 ± 47	Not measured due to excessive pull out	114 ± 28
20	2.2 ± 0.3	127 ± 34	1.2 ± 0.3	108 ± 22	Not measured due to excessive pull out	153 ± 29	Not measured due to excessive pull out	159 ± 17

for 20 h at 1450 °C (Fig. 3c), whereas in the absence of yttria the intergranular particles coarsened beyond ~2 μm in size following the same heat treatment (Fig. 3d and Table 1). Fig. 4a shows more clearly that the intergranular particles formed during aging of the yttria-doped solid solutions (A10FY) were finer by a factor of ~2 compared to the intergranular particles formed during aging of the A10F solid solutions for the same durations at 1450 °C. In contrast, the sizes of the nanosized (70–100 nm) intragranular particles, which precipitated after 10 h of aging, were similar in size with or without doping with yttria (Fig. 4b and Table 1). TEM observations also show the presence of relatively finer intergranular particles in the nanocomposites developed by aging of the yttria-doped solid solutions (A10FY) (Fig. 5a), as compared to those in the nanocomposites developed by aging of the A10F solid solutions for the same durations (Fig. 5b). No apparent effect of yttria doping on the average sizes of the intragranular nanoparticles could be observed even in the TEM micrographs.

As against the notable effect of yttria doping on the microstructural development during aging at 1450 °C, yttria addition did not have any apparent effect on the microstructural development during aging at the higher temperature of 1550 °C. Extremely coarse intergranular $FeAl_2O_4$ particles (~3 μm) were formed in the presence (Fig. 3e) as well as absence (Fig. 3f) of yttria during the initial stages of aging at 1550 °C, followed by rapid growth during continued aging (Table 1). In fact, after just 10 h of aging at 1550 °C, the development of a coarse and interconnected network of intergranular $FeAl_2O_4$ particles resulted in considerable pullout of these particles during metallographic polishing, which did not allow estimation of the particle sizes.

It has been observed that aging for 20 h leads to a volume fraction of precipitates which is close to the maximum volume fraction of $FeAl_2O_4$ (21 vol.%) that can be obtained on reduction of the Al_2O_3–10 vol.% Fe_2O_3 solid solutions. The addition of Y_2O_3 only slightly reduces the final volume fraction of the precipitates at the matrix grain boundaries. Table 2 presents the ratios of the volume fractions occupied by the intra- and intergranular $FeAl_2O_4$ particles in the nanocomposites developed on aging of the A10F and A10FY solid solutions at 1450 °C. The relative amounts of the intragranular nanosized particles, with respect to the coarser intergranular particles, increase with aging duration up to 20 h. The important observation is that for smaller aging times (before full precipitation has occurred) the precipitation rate at the grain boundaries is slowed significantly by Y_2O_3 doping, resulting in the generation of a relatively higher volume fraction within the grains (R) for a given aging time. In fact, a higher volume fraction of intragranular particles as compared to intergranular particles can be achieved on aging A10FY for a duration of 20 h or more. However, such effect progressively diminishes with increase in aging duration up to 50 h.

Table 2
Ratios of volume fractions of intragranular particles to volume fraction of intergranular particles (R) obtained during reduction aging of the yttria-free (A10F) and yttria-doped (A10FY) solid solutions at 1450 °C.

Aging durations at 1450 °C (h)	R obtained during aging of yttria-free (A10F) solid solutions	R obtained during aging of yttria-doped solid solutions (A10FY)
0	0	0
5	0	0.2 ± 0.07
10	0.3 ± 0.07	0.7 ± 0.02
15	0.5 ± 0.04	1.0 ± 0.08
20	0.9 ± 0.06	1.2 ± 0.14
50	0.9 ± 0.11	1.1 ± 0.09

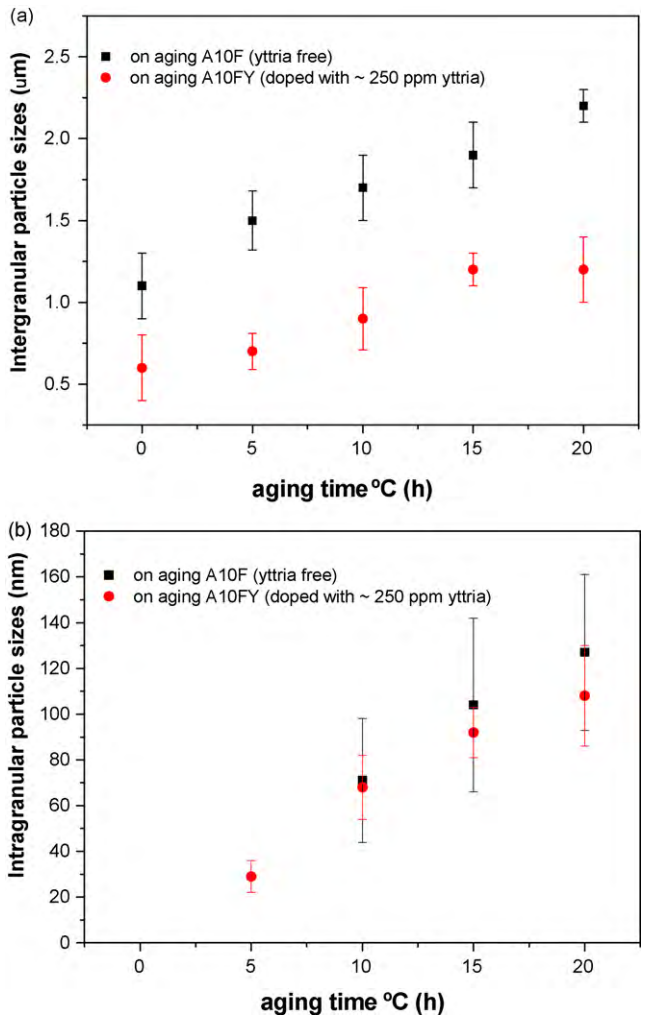

Fig. 4. Variation in the size of the (a) intergranular precipitate ($FeAl_2O_4$) particles and (b) intragranular precipitate particles with aging duration during reduction aging of the A10F and A10FY solid solutions at 1450 °C.

3.2. Mechanical properties of the Al_2O_3–$FeAl_2O_4$ nanocomposites

3.2.1. Hardness

The variations of the room temperature hardness with aging time at the two aging temperatures are presented in Fig. 6. Incorporation of Fe as solid solution resulted in reduction in hardness

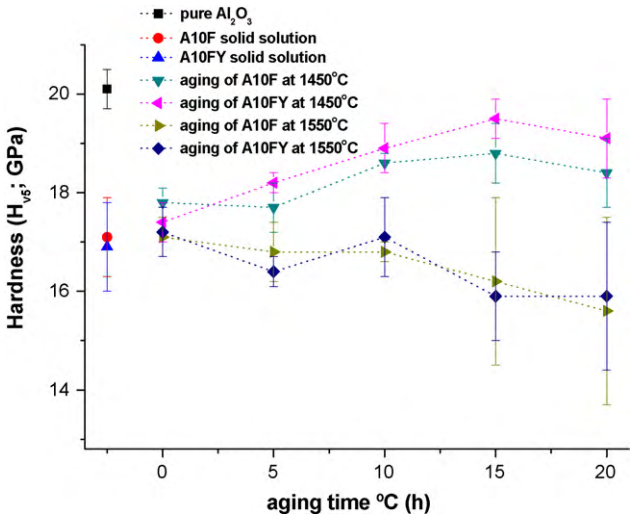

Fig. 6. Variation in hardness with aging durations during aging of A10FY and A10FY at 1450 and 1550 °C.

(~17 GPa), with respect to pure Al_2O_3 (~20 GPa). Aging of both the solid solutions (A10F and A10FY) at both the temperatures (1450 and 1550 °C) for 0 h did not lead to any apparent change in the hardness with respect to the solid solutions. Contrasting behaviour was observed during continued aging at the two different temperatures. During aging at 1450 °C the hardness increased with increase in aging durations up to >19 GPa (after 15 h), which was nearly comparable to that of pure Al_2O_3. It was also observed that the nanocomposites developed on aging the yttria-doped solid solutions possessed slightly higher hardness with respect to the nanocomposites developed by aging of the A10F solid solutions. On the contrary, the hardness got further reduced on aging at the higher temperature of 1550 °C, with yttria doping having no apparent effect.

3.2.2. Fracture toughness and flexural strength

Fig. 7 presents the room temperature fracture toughness (K_{Ic}) and flexural strength (σ_f) results. The toughness and strengths of both the solid solutions (A10F and A10FY) were similar to that of pure Al_2O_3. A modest increase in the fracture toughness (by ~0.3 MPa $m^{1/2}$), with respect to that of pure Al_2O_3, was obtained on aging the A10F solid solution at 1450 °C for 0 h (Fig. 7b). However, an insignificant improvement in fracture toughness

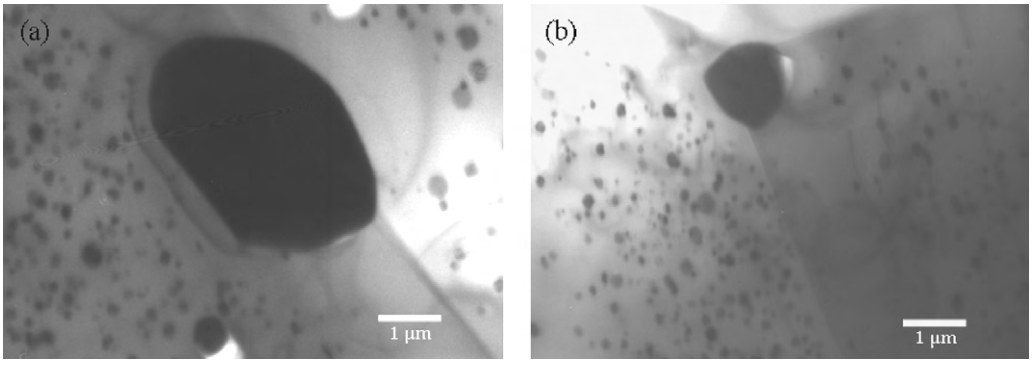

Fig. 5. Typical bright field TEM images obtained from nanocomposites developed on aging for 20 h at 1450 °C of (a) A10F and (b) A10FY solid solutions.

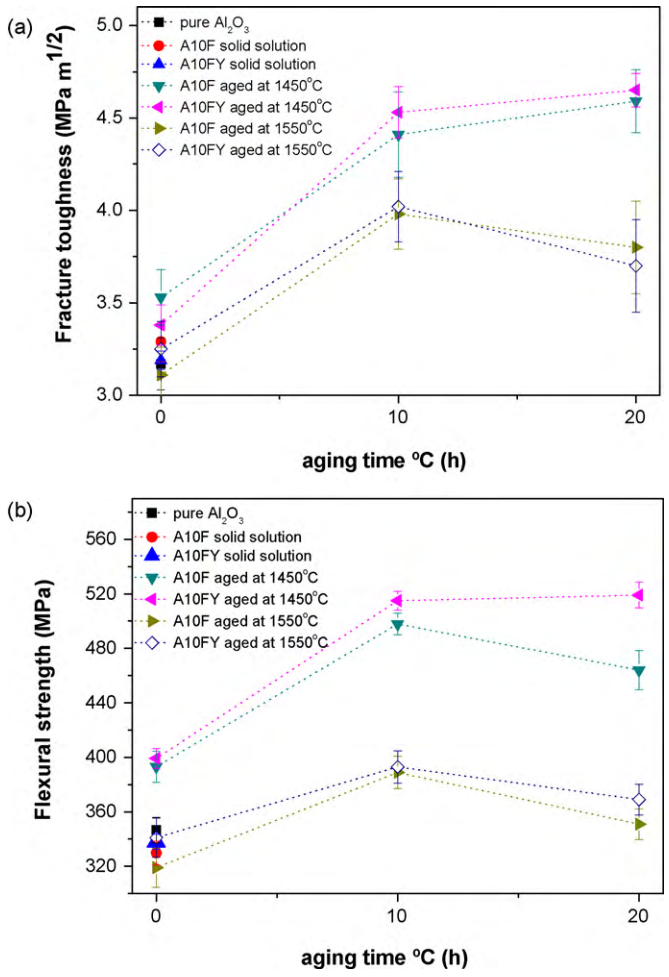

Fig. 7. The variation of (a) fracture toughness and (b) flexural strength with aging durations for the nanocomposites developed on reduction aging of yttria-free (A10F) and yttria-doped (A10FY) Al_2O_3–10 wt.% Fe_2O_3 solid solutions.

was obtained on aging the yttria-doped solid solution for the same duration (0 h) at 1450 °C. With increase in aging duration up to 20 h, the fracture toughness was observed to improve significantly for the nanocomposites developed from both the solid solutions (A10F and A10FY). A maximum improvement of fracture toughness by ~45% (K_{Ic} = 4.7 MPa m$^{1/2}$), with respect to pure Al_2O_3, was obtained on aging the A10FY solid solution for 20 h at 1450 °C. As against aging at 1450 °C, no improvement in fracture toughness was observed on aging for 0 h at 1550 °C in the presence or absence of yttria. With continued aging, a modest improvement in fracture toughness was observed after 10 h at 1550 °C. However, the improvement was considerably lower than those obtained on aging for the same duration at 1450 °C. On aging for a still longer duration of 20 h, a modest reduction in the fracture toughness was observed. Similar to aging at 1450 °C, yttria addition did not have any notable effect on the fracture toughness improvements achieved after aging at 1550 °C.

The flexural strength was found to improve considerably on aging both the solid solutions at 1450 °C, especially for 10 and 20 h (Fig. 7b). Though yttria addition did not have any effect on the strength improvement obtained on aging for 0 h, the strengths of the nanocomposites developed by continued aging were further improved in the presence of yttria doping. In particular, aging of A10FY for 20 h did not lead to any deterioration of strength with respect to that obtained on aging for 10 h, which is contrary to that observed on aging of A10F. The strength of the nanocomposite developed on aging the yttria-doped solid solution for 20 h at 1450 °C was higher by ~55 MPa, with respect to the nanocomposite developed by aging A10F for the same duration. Hence, a maximum improvement in flexural strength of ~50% (σ_f ~ 520 MPa) over that of monolithic Al_2O_3 was obtained with the nanocomposite developed on aging A10FY for 20 h at 1450 °C.

3.3. Observation of fractured surfaces

The fractured surfaces obtained during fracture toughness testing of monolithic Al_2O_3, the solid solutions (A10F and A10FY) and the nanocomposites developed by reduction aging were observed in SEM. Representative images are presented in Fig. 8. Monolithic Al_2O_3 exhibited the classical intergranular fracture mode. No change in fracture mode was observed with respect to that of monolithic Al_2O_3 on incorporation of Fe_2O_3 as solid solution, in the presence (Fig. 8a) or absence of yttria. Furthermore, aging of both the solid solutions for 0 h at both the temperatures also did not have any apparent effect on the fracture mode (Fig. 8b). By contrast, aging of A10F and A10FY for 10 and 20 h at both the temperatures resulted in an almost complete change in the fracture mode to transgranular fracture (Fig. 8c and d). Though the nanosized intragranular particles did not fall out during the fracture process, holes left due to the loss of the coarser intergranular particles were frequently observed on the fractured surfaces (see Fig. 8d). There was no notable effect of yttria content on the fracture mode for any of the materials studied.

4. Discussion

4.1. Factors controlling the rate of precipitation

It has been demonstrated that reduction of the dissolved Fe^{3+} in the Al_2O_3–Fe_2O_3 solid solutions to Fe^{2+} during aging in the reducing atmosphere results in the precipitation of Fe^{2+}-containing second phase particles ($FeAl_2O_4$) due to the low solubility of Fe^{2+} in Al_2O_3.[29] In our earlier paper,[19] we proposed chemical reactions for the formation of $FeAl_2O_4$. The fact that the precipitation of $FeAl_2O_4$ occurs uniformly throughout the thickness of the specimen suggests that the rate of these reactions is controlled by the local atomic rearrangements required rather than the supply of the reducing species or diffusion of oxygen out of the specimen.

Figs. 3–5 and Table 1 show that the main effect of the Y_2O_3 is on the kinetics of precipitate development at the matrix grain boundaries. There is no evidence of a strong effect of the Y_2O_3 on the nucleation of the grain boundary particles, but both the overall rate of precipitation and the coarsening rate are clearly reduced. The much smaller effect of the Y_2O_3 additive on the relative volume fractions of precipitates at the grain boundary

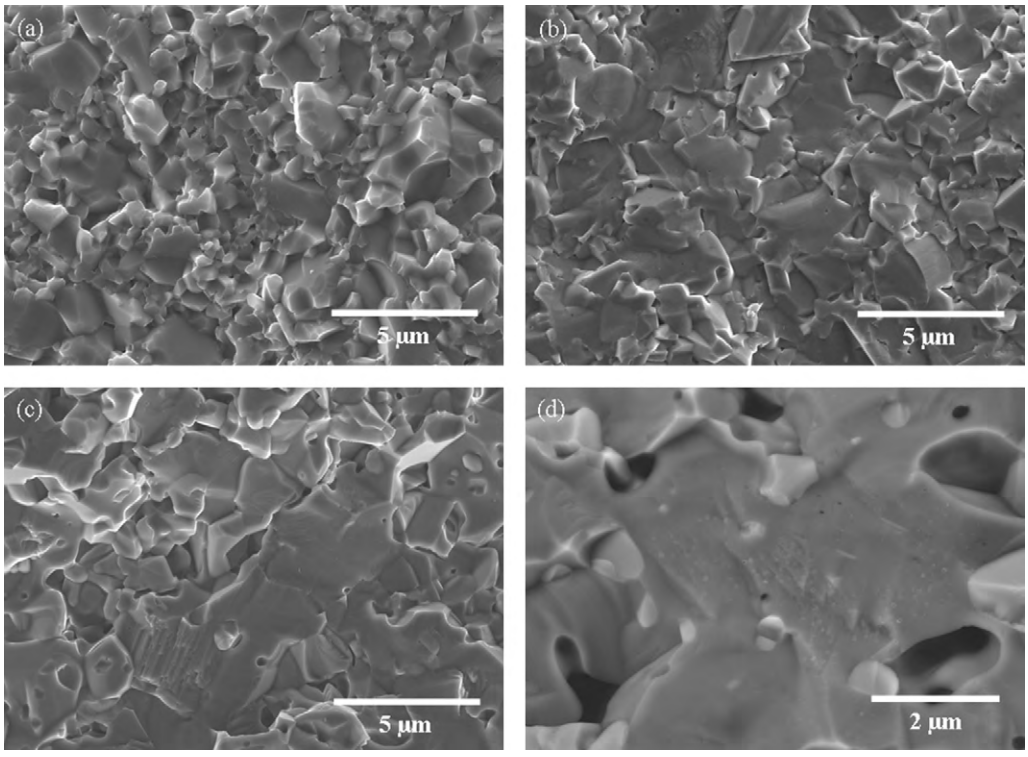

Fig. 8. SEM images obtained with fractured surfaces of nanocomposites developed by reduction aging A10FY at (a) 1550 °C for 0 h; (b) 1450 °C for 20 h and (c) 1550 °C for 20 h. (d) A higher magnification BSE-SEM image of the fractured surface of nanocomposite developed on aging A10FY at 1550 °C for 10 h, which shows the intact nanosized intragranular second phase particles and the holes created due to fall out of the intergranular particles.

and within the grains after long periods of aging (see Table 2) may be because the amount of Fe available to the grain boundary is related to the width of the precipitate free zone, and must depend on $(D_{\text{eff}}t)^{1/2}$, where D_{eff} is the effective diffusion coefficient in the crystal lattice for the rate controlling species and t is the aging time.

Similar arguments may also explain why aging at 1550 °C is less successful in developing the required microstructure than 1450 °C. If the nucleation rate of precipitates within the grains is accelerated less by the increase in temperature than D_{eff}, more Fe can diffuse to the grain boundary precipitates before a substantial volume fraction of intragranular particles has time to develop. Although the above considerations give plausible rationalisation for the observed behaviour, a fuller understanding of the microstructural development requires a more detailed investigation of the interaction between the rates of reduction, nucleation, growth and coarsening of the particles on the grain boundaries and within the grains.

4.2. *Effect of microstructural development on the mechanical properties*

The results show that the incorporation of Fe_2O_3 in solid solution in Al_2O_3 lowered the hardness considerably. In an earlier work, Kennedy and Bradt[30] had also observed similar solid solution softening of polycrystalline Al_2O_3, where the hardness was observed to decrease from 20 GPa for pure Al_2O_3 with an increase in solute concentration, reaching a hardness of ~18 GPa on the incorporation of 2 mol% $MgO.TiO_2$ in solution. During reduction aging of the present Al_2O_3–Fe_2O_3 solid solutions, the precipitation of micron (for A10F) and sub-micron (for A10FY) sized intergranular $FeAl_2O_4$ particles only (0 h aging) did not lead to any noticeable change in the hardness, whereas the precipitation of nanosized intragranular $FeAl_2O_4$ particles increased the hardness with respect to the solid solutions. Doping with yttria maximised the improvement in hardness on aging and this may be correlated with the presence of finer intergranular particles in the yttria-doped samples (see Table 2 and Fig. 4). The increase in hardness on aging at 1450 °C appears at first sight to be a classical precipitation hardening response. A maximum increase in uniaxial yield stress ($\Delta\sigma_y$) from this effect can be estimated by assuming that the dislocations bow around the precipitates, so that;

$$\Delta\sigma_y = \frac{2Gb}{L} \tag{3}$$

where b is the Burgers Vector, G the shear modulus and L is the spacing between the precipitate particles. The factor of 2 arises in converting from shear stress to uniaxial yield stress. Taking $G = 160$ GPa, $b = 0.2$ nm and $L = 200$ nm, Eq. (3) gives a value of 320 MPa for $\Delta\sigma_y$. Assuming that $\Delta H_v \sim 3\Delta\sigma_y$, a hardness increment of 0.96 GPa is predicted based on the above analysis. This is less than the observed maximum hardness increment of ~2.5 GPa during aging. It is therefore believed that much of the hardness increase on aging is a consequence of the accompanying removal of Fe^{3+} from the solid solution.

In contrast to the modest hardness improvements observed during aging of the solid solutions at 1450 °C, the hardness

was observed to deteriorate with time during aging at 1550 °C. We believe that the formation of extremely coarse micron-sized intergranular particles during aging at 1550 °C (see Table 1) nullified the effect of the nanosized intragranular particles. It has been reported earlier that second phase particles larger than a certain size are often prone to spontaneous microcracking at their interfaces with the matrix[31–36] and such microcracking is also responsible for reduction in hardness for brittle materials like ceramics.[33]

The present results indicate that the formation of $FeAl_2O_4$ as second phase particles during aging results in an increase in fracture toughness, with the degree of improvement depending on the aging duration and concomitantly on the size and distribution of the second phase particles. One mechanism for toughness increase in particulate reinforced ceramic composites arises from the development of CTE mismatch-induced residual stresses.[2,37–39] In the nanocomposites under investigation, the second phase particles ($FeAl_2O_4$) have higher thermal expansion co-efficient ($\alpha_p \sim 13 \times 10^{-6}\,K^{-1}$)[40] than the matrix ($Al_2O_3$; $\alpha_m \sim 8 \times 10^{-6}\,K^{-1}$)[40,41]. This is likely to result in the development of residual compressive stresses in the matrix during cooling from the heat treatment temperatures. According to a theory proposed by Taya et al.,[37] development of such compressive residual stresses in the matrix can result in the toughening of particulate reinforced ceramic composites.

The model[37] is based on the misfit strain (ε) that develops in the particles due to the co-efficient of thermal expansion (CTE) mismatch and which is given by

$$\varepsilon = \int_{T_P}^{T_R} (\alpha_p - \alpha_m)\,dT \tag{4}$$

where T_p is the temperature below which plasticity is considered to be negligible ~1000 °C and T_R is room temperature. The isotropic average stress fields in the particles and matrix are given by $\langle\sigma\rangle_p$ and $\langle\sigma\rangle_m$, respectively, which can be estimated for a given volume fraction of second phase particles (f_p) according to the following equations:

$$\frac{\langle\sigma\rangle_p}{E_m} = \frac{-2(1-f_p)\beta\varepsilon}{A} \tag{5}$$

and

$$\frac{\langle\sigma\rangle_m}{E_m} = \frac{2f_p\beta\varepsilon}{A} \tag{6}$$

where,

$$A = (1-f_p)(\beta+2)(1+\nu_m) + 3\beta f_p(1-\nu_m) \tag{7}$$

$$\beta = \left(\frac{1+\nu_m}{1+\nu_p}\right)\left(\frac{E_p}{E_m}\right) \tag{8}$$

where ν_m and E_m are Poisson's ratio (0.23) and Young's modulus (400 GPa) for the matrix (Al_2O_3),[42] and ν_p and E_p are Poisson's ratio (0.3) and Young's modulus (225 GPa) of the second phase particles ($FeAl_2O_4$).[43,44]

In the case of the composite developed on aging A10F for 0 h at 1450 °C, considering f_p as 0.1 (see Fig. 3) and using Eqs. (5)–(9), the residual stress in the matrix can be estimated as; $\langle\sigma\rangle_m = -143.5$ MPa. It may be recalled here that this composite contains only intergranular micron-sized second phase particles (see Fig. 3a). According to Taya et al.,[37] the existence of such compressive residual stresses in the matrix of particulate reinforced composites increases the apparent fracture toughness by ΔK_{Ic}, given by:

$$\Delta K_{Ic} = 2\langle\sigma\rangle_m\sqrt{\frac{2(\lambda-d)}{\pi}} \tag{9}$$

where λ is the interparticle distance and d is the average diameter of the second phase particles. Considering λ as 4 μm (see Fig. 3a) and d as 1 μm (see Table 1) for the composite developed on aging for 0 h, Eq. (9) predicts a fracture toughness increase of ~0.4 MPa $m^{1/2}$; which agrees reasonably well with the experimentally measured (via SEVNB) fracture toughness increment of ~0.3 MPa $m^{1/2}$ over that of monolithic Al_2O_3 (see Fig. 7a). Hence for the composite developed on aging for a duration of 0 h and characterised by the presence of only intergranular second phase particles, the modest toughening effect due to the presence of thermal residual stress seems to be the major contributor.

The precipitation of nanosized intragranular $FeAl_2O_4$ particles on aging for 10 h or more at 1450 °C was accompanied by a much greater increment in fracture toughness (see Figs. 3, 4 and 7). The additional contribution towards such residual stress induced toughening solely by the nanosized intragranular particles (volume fraction ~0.09), in the nanocomposite developed on aging for a duration of 20 h, can be estimated to be only ~0.2 MPa $m^{1/2}$ using Eqs. (5)–(10). Hence, toughening based on thermal expansion mismatch-induced residual stresses alone cannot account for the experimentally observed fracture toughness increment of ~1.5 MPa $m^{1/2}$ for the inter/intragranular nanocomposite. Hence, some additional toughening mechanism must be operative in the presence of nanosized intragranular particles.

It must be recalled here that the change in fracture mode from intergranular to transgranular for the nanocomposites coincided with the appearance of the nanosized intragranular particles during reduction aging for 10 h or more at 1450 °C. Hansson et al.[45] found similar toughness increments with the addition of SiC whiskers to alumina. The SiC whiskers also caused a change in fracture mode. A detailed consideration of the trade off between the increased toughness of the grain interior relative to the grain boundary and the reduction in crack deflection in the flatter, transgranular fracture mode showed that the net increase in toughness of 1.2–2.3 MPa $m^{1/2}$ could be explained in this way. We conclude, therefore, that the change in fracture mode on precipitation of the intragranular nanoparticles is the likely explanation for the accompanying toughening increments in the range found in this work.

An important observation is that the variation in flexural strength of the nanocomposites with aging schedules scaled quite well with the corresponding variations in the fracture toughness. This implies that the strength of the present in situ nanocomposites is not limited by other factors such as the presence of processing defects which often limit the strength improvement with mixed powder routes for nanocomposite

production.[4] It has also been observed that the effect of yttria addition on the strength improvement becomes more pronounced with increasing aging duration at 1450 °C (see Fig. 7b). We believe that this is due to the role of yttria in limiting the growth of the intergranular particles to a size of ~1 μm, beyond which they are deleterious towards the strength. It has been frequently observed that the coarser intergranular particles get pulled out during polishing (Fig. 3e and f) and fall off during fracture (Fig. 8d), while the nanosized intragranular particles and the intergranular particles of size less than 2 μm remain intact. The $FeAl_2O_4$ particles here are in a state of tensile residual stress and it is well known that microcracking in these conditions is more prevalent with larger particles.[31] On a similar note, the presence of such coarse intergranular particles, even in the presence of yttria, is presumably responsible for the significantly lower flexural strength of the nanocomposites developed during aging at 1550 °C.

5. Conclusions

The present work has investigated the effect of yttria doping on the microstructural development and mechanical properties of Al_2O_3–$FeAl_2O_4$ nanocomposites developed via solution precipitation.[19,20] More precisely,

(a) Incorporation of ~250 ppm by weight of Y_2O_3 in the Al_2O_3–10 wt.% Fe_2O_3 (A10F) solid solutions resulted in suppression of the growth of intergranular $FeAl_2O_4$ particles during reduction aging (in N_2 + 4% H_2) at 1450 °C. The sizes of the intergranular particles were reduced by a factor of ~2 with respect to those obtained on aging of the yttria-free solid solution (A10F) for the same durations at 1450 °C. The addition of yttria did not have any significant effect on the formation and growth of the nanosized $FeAl_2O_4$ particles within the alumina grains.
(b) No effect of yttria addition on the growth of the intergranular particles was observed on aging at the higher temperature of 1550 °C. This resulted in the formation of coarse micron-sized inter-connected network of intergranular particles on aging the solid solutions at 1550 °C.
(c) The incorporation of yttria resulted in a modest improvement in the hardness of the optimum nanocomposites with respect to the nanocomposites developed with the same aging schedules in the absence of yttria.
(d) The nanocomposites developed on optimum aging in the presence of yttria possessed considerably improved fracture toughness (by ~45%) and flexural strength (by ~50%) with respect to monolithic Al_2O_3. The change in fracture mode from intergranular to transgranular in the presence of the nanosized intragranular particles is believed to be the major contribution towards improvement in fracture toughness and strength.
(e) In general, the yttria-doped samples showed improved properties after aging with respect to the yttria-free samples and the effect of yttria became more pronounced with increase in aging duration. This was attributed to the reduction in size of the intergranular $FeAl_2O_4$ particles on adding Y_2O_3.

References

1. Niihara K. New design concept of structural ceramics. *J Ceram Soc Jpn* 1991;**99**:974–82.
2. Mukhopadhyay A, Basu B. Consolidation-microstructure-properties of bulk nanoceramics and ceramic nanocomposites: a review. *Int Mater Rev* 2007;**52**(4):1–32.
3. Mukhopadhyay A. Tribological properties and processing challenges of bulk structural ceramic nanomaterials. *Tribol—Mater Surf Interfaces* 2008;**2**(3):169–84.
4. Sternitzke M. Review: structural ceramic nanocomposites. *J Eur Ceram Soc* 1997;**17**:1061–82.
5. Ortiz Merino JL, Todd RI. Relationship between wear rate, surface pull-out and microstructure during abrasive wear of alumina and alumina/SiC nanocomposites. *Acta Mater* 2005;**53**:3345–57.
6. Limpichaipanit A, Todd RI. The relationship between microstructure, fracture and abrasive wear in Al_2O_3/SiC nanocomposites and microcomposites containing 5 and 10% SiC. *J Eur Ceram Soc* 2009;**29**:2841–8.
7. Walker CN, Borsa CE, Todd RI, Davidge RW, Brook RJ. Fabrication, characterisation and properties of alumina matrix nanocomposites. *Br Ceram Proc* 1994;**53**:249–64.
8. Zhao J, Stearns LC, Harmer MP, Chan HM, Miller GA, Cook RF. Mechanical behavior of alumina–silicon carbide "nanocomposites". *J Am Ceram Soc* 1993;**76**:503–10.
9. Stearns LC, Zhao J, Harmer MP. Processing and microstructure development in Al_2O_3–SiC 'nanocomposites'. *J Eur Ceram Soc* 1992;**10**:473–7.
10. Chen HJ, Rainforth WM, Lee WE. The wear behaviour of Al_2O_3–SiC ceramic nanocomposites. *Scripta Mater* 2000;**42**:555–60.
11. Davidge RW, Twigg PC, Riley FL. Effects of silicon carbide nano-phase on the wet erosive wear of polycrystalline alumina. *J Eur Ceram Soc* 1996;**16**:799–802.
12. Basu B, Venkateswaran T, Sarkar D. Pressureless sintering and tribological properties of WC–ZrO_2 composites. *J Eur Ceram Soc* 2005;**25**:1603–10.
13. Jeong YK, Nakahira A, Niihara K. Effects of additives on microstructure and properties of alumina–silicon carbide nanocomposites. *J Am Ceram Soc* 1999;**92**:3609–12.
14. Cock AM, Shapiro IP, Todd RI, Roberts SG. Effects of yttrium on the sintering and microstructure of alumina–silicon carbide "nanocomposites". *J Am Ceram Soc* 2005;**88**:2354–61.
15. Zhang FC, Luo HH, Roberts SG, Todd RI. Effect of fracture mode on wear resistance of alumina-based ceramics. *J Inorg Mater* 2007;**22**:493–8.
16. Burgos-Montes O, Moreno R, Baudín C. Effect of mullite additions on the fracture mode of alumina. *J Eur Ceram Soc* 2010;**30**:857–63.
17. Wang Y, Fujimoto T, Maruyama H, Koga K. Precipitation of magnesium aluminum spinel from alumina-matrix solid solution: I. Fundamental concept and precipitation behavior. *J Am Ceram Soc* 2000;**83**(4):933–6.
18. Langensiepen RA, Tressler RE, Howell PR. A preliminary study of precipitation in Ti^{4+}-doped polycrystalline alumina. *J Mater Sci* 1983;**18**:2771–6.
19. Mukhopadhyay A, Todd RI. Microstructure and mechanical properties of Al_2O_3 matrix nanocomposites developed via solid state precipitation. *J Eur Ceram Soc* 2010;**30**:1359–72.
20. Mukhopadhyay A, Todd RI. Production of Alumina matrix nanocomposites by solid state precipitation. Ceram. Eng. Sci. Proc. 2010; 30(7). In: Mathur S, Singh M, editors. Nanostructured Materials and Nanotechnology III; p. 119-31.
21. Lee HY, Paek YK, Lee BK, Kang SJL. Discontinuous dissolution of iron aluminate spinel in the Al_2O_3–Fe_2O_3 system. *J Am Ceram Soc* 1995;**78**(8):2149–52.
22. Korinek SL, Carry C, Priester L. Multiscale aspects of the influence of yttrium on microstructure, sintering and creep of alumina. *J Eur Ceram Soc* 2002;**22**:1525–41.
23. Lartigue S, Carry C, Priester L. Grain boundaries in high temperature deformation of yttria and magnesia co-doped alumina. *J Phys (Paris), C1* 1990;**51**:985–90.

24. Cho J, Harmer MP, Chan HM, Rickman JM, Thompson AM. Effect of yttrium and lanthanum on the tensile creep behavior of aluminium oxide. *J Am Ceram Soc* 1997;**80**(4):1013–7.
25. Loudjani MK, Haut C. Influence of the oxygen pressure on the chemical state of yttrium in polycrystalline α-alumina. relation with microstructure and mechanical toughness. *J Eur Ceram Soc* 1996;**16**:1099–106.
26. dash;S French JD, Zhao, Harmer MP, Chan HM, Miller GA. Creep of duplex microstructures. *J Am Ceram Soc* 1994;**77**:2857–65.
27. Coble RL. Sintering crystalline solids. II. Experimental test of diffusion models in powder compacts. *J Appl Phys* 1961;**32**(5):793–9.
28. Mizuno M, Okuda H. VAMAS round robin on fracture toughness of silicon nitride. *J Am Ceram Soc* 1995;**78**:1793–801.
29. Tartaj J, Messing GL. Anisotropic grain growth in α-fe_2o_3 doped alumina. *J Eur Ceram Soc* 1997;**17**:719–25.
30. Kennedy CR, Bradt RC. Softening of Al_2O_3 by solid solution of $MgO{\cdot}TiO_2$. *J Am Ceram Soc* 1973;**56**:608.
31. Davidge RW, Green TJ. The strength of two-phase ceramic/glass materials. *J Mater Sci* 1968;**3**:629–34.
32. Rice RW, Pohanka RC. Grain-size dependence of spontaneous cracking in ceramics. *J Am Ceram Soc* 1979;**62**:559–63.
33. Mukhopadhyay A, Raju GB, Basu B, Suri AK. Correlation between phase evolution, mechanical properties and instrumented indentation response of TiB_2-based ceramics. *J Eur Ceram Soc* 2009;**29**:505–16.
34. Evans AG. The role of inclusions in the fracture of ceramic materials. *J Mater Sci* 1974;**9**:1145–52.
35. Weyl D. Influence of internal strains on the texture and mechanical strength of porcelains. *Ber Deut Keram Ges* 1959;**36**:319–24.
36. Selsing J. Internal stresses in ceramics. *J Am Ceram Soc* 1961;**44**:419.
37. Taya M, Hayashi S, Kabayashi AS, Yoon HS. Toughening of a particulate-reinforced ceramic-matrix composite by thermal residual stresses. *J Am Ceram Soc* 1990;**73**:1382–91.
38. Raju GB, Basu B. Densification, sintering reactions and properties of titanium diboride with titanium disilicide as a sintering aid. *J Am Ceram Soc* 2007;**90**(11):3415–23.
39. Ohji T, Jeong YK, Choa YH, Niihara K. Strengthening and toughening mechanisms of ceramic nanocomposites. *J Am Ceram Soc* 1998;**81**(6):1453–60.
40. Fujimura T, Tanaka SI. In-situ high temperature X-ray diffraction study of Fe/Al_2O_3 interface reactions. *J Mater Sci* 1999;**34**:425–9.
41. Ishizawa N, Miyata T, Minato I, Marumo F, Iwai S. A Structural Investigation of α-Al_2O_3 at 2170 K. *Acta Crystallogr Sect B: Struct Sci* 1980;**36**:228–30.
42. Munro RG. *Elastic moduli data for polycrystalline ceramics*. Gaithersburg, MD 20899: NISTIR 6853; 2002.
43. Reichmann HJ, Jacobsen SD. Sound velocities and elastic constants of $ZnAl_2O_4$ spinel and implications for spinel-elasticity systematics. *Am Mineral* 2006;**91**:1049–54.
44. Wang H, Simmons G. Elasticity of some mantle crystal structures 1. Pleonaste and hercynite spinel. *J Geophys Res* 1972;**77**:4379–92.
45. Hansson T, Warren R, Wasen J. Fracture toughness anisotropy and toughening mechanisms of a hot-pressed alumina reinforced with silicon carbide whiskers. *J Am Ceram Soc* 1993;**76**(4):841–8.